A&A 560, A14 (2013)
DOI: 10.1051/0004-6361/201322214

Astronomy & Astrophysics

The external origin of the polar gaseous disk of the S0 galaxy IC 5181⋆,⋆⋆

A. Pizzella[1,2], L. Morelli[1,2], E. M. Corsini[1,2], E. Dalla Bontà[1,2], and M. Cesetti[1]

[1] Dipartimento di Fisica e Astronomia "G. Galilei", Università di Padova, vicolo dell'Osservatorio 3, 35122 Padova, Italy
e-mail: alessandro.pizzella@unipd.it
[2] INAF – Osservatorio Astronomico di Padova, vicolo dell'Osservatorio 5, 35122 Padova, Italy.

Received 5 July 2013 / Accepted 19 September 2013

ABSTRACT

Context. Galaxies accrete material from the environment through acquisition and merging events. These processes contribute to galaxy assembly and leave their fingerprints on the galactic morphology, internal kinematics of gas and stars, and stellar populations.
Aims. We study the nearby S0 galaxy IC 5181 to address the origin of the ionized gas component that orbits the galaxy on polar orbits.
Methods. We measure the surface brightness distribution of the stars and ionized gas of IC 5181 from broadband and narrow-band imaging. The structural parameters of the galaxy are obtained with a photometric decomposition assuming a Sérsic and exponential profile for the bulge and disk, respectively. We measure the ionized-gas and stellar kinematics and the line strengths of the Lick indices of the stellar component along both the major and minor axis. The age, metallicity, and [α/Fe] enhancement of the stellar populations are derived using single stellar population models with variable element abundance ratios. The ionized-gas metallicity is obtained from the equivalent width of the emission lines.
Results. The galaxy IC 5181 is a morphologically undisturbed S0 galaxy with a classical bulge made by old stars with super solar metallicity and overabundance. Stellar age and metallicity decrease in the disk region. The galaxy hosts a geometrically and kinematically decoupled component of ionized gas. It is elongated along the galaxy minor axis and in orthogonal rotation with respect to the galaxy disk.
Conclusions. We interpret the kinematical decoupling as suggesting that there is a component of gas, which is not related to the stars and having an external origin. The gas was accreted by IC 5181 on polar orbits from the surrounding environment.

Key words. galaxies: photometry – galaxies: kinematics and dynamics – galaxies: stellar content – galaxies: individual: IC 5181 – galaxies: formation

1. Introduction

It is widely accepted that galaxies undergo a number of acquisition and merging events during their assembly and growth. Depending on the nature and mass of the accreted material and the geometry and duration of the accretion process, such events may leave temporary or permanent signatures in the morphology, kinematics, and stellar populations of the host galaxy (see the reviews by Rubin 1994; Schweizer 1998; and Bertola & Corsini 1999). Some examples of the features observed in lenticular and spiral galaxies are the counter-rotating disks of gas (Ciri et al. 1995; Chung et al. 2012), counter-rotating disks of stars (Rubin et al. 1992; Bertola et al. 1996), nuclear polar disks (Corsini et al. 2003; Sil'chenko & Afanasiev 2004), large-scale polar rings (Whitmore et al. 1990; Moiseev et al. 2011), polar bulges (Bertola et al. 1999; Matthews & de Grijs 2004), and nuclear stellar disks (Krajnović & Jaffe 2004; Corsini et al. 2012).

Lenticular galaxies are gas-poor systems (Haynes et al. 1984). Several pieces of evidence suggest that the origin of gas is external in at least a fair fraction of S0s and not only in some peculiar cases. Assuming gas infall with randomly oriented angular momentum, Bertola et al. (1992) found that the ionized gas is of external origin in about 40% of the S0 galaxies in their sample. This result has been confirmed by Kuijken et al. (1996), who set the fraction of S0s with retrograde gas to 24 ± 10%. More recently, studying a large sample of fast-rotating early-type galaxies, Davis et al. (2011) found that 42 ± 5% of galaxies show decoupling between the stellar and gaseous components.

Counter-rotating gaseous disks are observed in less than 12% of spiral galaxies, and only a few of them host a significant fraction of counter-rotating stars (Kannappan & Fabricant 2001; Pizzella et al. 2004). The comparison to S0 galaxies suggests that the retrograde acquisition of small amounts of external gas gives rise to counter-rotating gaseous disks only in S0s, while the newly acquired gas in gas-rich spirals is swept away by the pre-existing gas. The gas from the environment interacts and dissipates with that of the host galaxy, and in most cases, it will not survive to build a counter-rotating component. Indeed, counter-rotating gaseous and stellar disks in spirals are formed only from the retrograde acquisition of large amounts of gas exceeding that of pre-existing gas and fueling a subsequent in situ star formation. The two counter-rotating stellar components are expected to have different stellar populations (Coccato et al. 2013; Katkov et al. 2013).

In addition, there are disk galaxies where the angular momenta of the main stellar body and decoupled gaseous component are even orthogonal to each other. This is the case of polar ring galaxies. The accretion of external material through the capture of gas clouds or merging with formed galaxies (Spavone et al. 2010; Combes et al. 2013) is also invoked to explain the

⋆ Based on observation collected at the European Southern Observatory for the programme 63.N-0327(A).
⋆⋆ Tables 1–3 are available in electronic form at http://www.aanda.org

formation of this class of relatively rare objects (Moiseev et al. 2011). The infall of massive gas clouds gives rise to the formation of large-scale polar disks of stars (Iodice et al. 2002). Inclined disks of stars and gas are also observed in lenticular galaxies (Sil'chenko et al. 2009). The stability of polar and inclined orbits in axisymmetric and triaxial potentials have been addressed from both a theoretical (e.g., Friedli & Benz 1993; Athanassoula 2003) and observational point of view (Pizzella et al. 1997; Emsellem et al. 2006; Bureau et al. 2006).

The galaxy IC 5181 is a large (2.′6 × 0.′8; de Vaucouleurs et al. 1991, hereafter RC3) and bright (B_T = 12.51; RC3) early-type disk galaxy. It is classified as an edge-on SA0 in RC3 and an $S0_1(7)$ in Sandage & Bedke (1994) due to the presence of a flattened thick disk. Its total absolute magnitude is $M^0_{B,T}$ = −19.48 which is corrected for inclination and extinction (RC3) and adopts a distance of 24.8 Mpc (Tully 1988). IC 5181 is a member of the loose NGC 7213 group (Maia et al. 1989; Garcia 1993). It forms a pair with the edge-on spiral galaxy NGC 7232A at 8.′1 separation, corresponding to a projected linear distance of 58.4 kpc.

In the framework of acquisition events occurred in the lifetime of galaxies, we present IC 5181 as a new case of a disk galaxy that is characterized by a geometric and kinematic orthogonal decoupling between its stellar body and the ionized-gas component. This paper is organized as follows: the photometric and spectroscopic observations of IC 5181 are presented in Sect. 2. The results about the measurements of the distribution, kinematics, and chemical properties of the stars and ionized gas are discussed in Sect. 3. The conclusions are given in Sect. 4.

2. Observations and data reduction

2.1. Narrow and broadband imaging

The photometric observations of IC 5181 were carried out at European Southern Observatory (ESO) in La Silla with the 2.2-m MPG/ESO telescope equipped with the Wide Field Imager (WFI) on July 22, 1999.

The galaxy was centered on the No. 51 EEV CCD, which has 2048 × 4096 pixels of 15 × 15 μm^2. It yielded a field of view of 8.′1 × 16.′2 with an image scale of 0.″238 pixel^{-1}. The gain and readout noise were 2.1 e$^-$ count^{-1} and 5.2 e$^-$ (rms), respectively. Two 300 s narrow-band images were obtained with the Hα/7 No. 856 filter to isolate the spectral region characterized by the redshifted Hα and [N II] $\lambda\lambda$6548, 6583 emission lines, according to the galaxy systemic velocity. One 30 s, two 300 s, and one 600 s images were taken with the Ic/Iwp No. 845 broadband filter to subtract off the stellar continuum from the emission-band images. The shortest exposure was taken to deal with the saturation of the galaxy nucleus thet resulted in the deeper broadband exposures. Since the night was characterized by good photometric conditions, some photometric standards were observed to calibrate the flux of broadband images.

The data reduction was performed using standard MIDAS[1] routines. All the images were bias subtracted and flat-field corrected. The sky level was determined in a number of regions selected to be empty areas far from IC 5181 to avoid the contamination of the target galaxy and of foreground and background sources. The broadband images were affected by fringing, which were corrected by subtracting the fringing-pattern frame made that is available to this aim by the ESO calibration plan of WFI. This reduced the fringing level from 5% to less than 1% of the sky level. No fringing correction was needed for the narrow-band images. The images were then shifted and aligned to an accuracy of a few hundredths of a pixel using common field stars as a reference. After comparing their point-spread functions (PSFs), the frames obtained with the same filter were combined to obtain a single narrow and single broadband image. The cosmic rays were identified and removed during the averaging process. The seeing full width half maximum (FWHM) of the resulting narrow and broadband image, as measured by fitting a two-dimensional Gaussian to the field stars, is 0.″7 and 0.″6, respectively. The broadband image was flux calibrated to the Cousins I-band. The photometric calibration constant includes only the correction for atmospheric extinction, which is taken from the differential aerosol extinction for ESO (Burki et al. 1995). No color term has been considered, and no attempt was made to correct for internal and Galactic extinction.

Finally, the broadband image was convolved with a Gaussian PSF to yield the same PSF FWHM of the narrow-band image. The broadband image was suitably scaled and subtracted from the narrow-band image to obtain a continuum-free map of the Hα+[N II] emission of the galaxy. The scale factor was estimated by comparing the surface brightness measured in the two pass-bands between 20″ and 30″ from the center. The resulting I-band and continuum-free images of IC 5181 are shown in Fig. 1.

2.2. Long-slit spectroscopy

The spectroscopic observations of IC 5181 were carried out at ESO in La Silla with the 1.52 m ESO telescope on June 9–11, 1999. The telescope was equipped with the Cassegrain Boller & Chivens spectrograph. The No. 33 grating with 1200 grooves mm^{-1} was used in the first order in combination with a 2.″2 × 4.′2 slit, and the No. 39 Loral/Lesser CCD, which has 2048 × 2048 pixels of 15 × 15 μm^2. The gain and readout noise are 1.2 e$^-$ count^{-1} and 5.4 e$^-$ (rms), respectively. The spectral range between about 4850 Å and 6850 Å was covered with a reciprocal dispersion of 0.98 Å pixel^{-1}. The spatial scale was 0.″81 pixel^{-1}. The instrumental resolution was 2.75 Å (FWHM), and it was derived from the mean of the Gaussian FWHM that were measured for a dozen unblended arc-lamp lines distributed over the whole spectral range of a wavelength-calibrated comparison spectrum. It corresponds to σ_{instr} = 53 km s^{-1} at Hα.

The galaxy IC 5181 was observed along the major (PA = 74°) and minor axis (PA = 164°). At the beginning of each exposure, the galaxy was centered on the slit using the guiding camera. Repeated exposures of 2700 s each ensured 1.5 and 3.0 h of effective integration along the major and minor axis, respectively, without storing up too many cosmic rays. Some spectro-photometric standard stars were observed to calibrate the flux of the spectra before line-strength indices were measured. Spectra of the comparison arc lamp were taken before and/or after object exposures. The value of the seeing FWHM during the observing nights, as measured by the La Silla Differential Image Motion Monitor (DIMM), ranged between 1.″0 and 1.″5.

All the spectra were bias subtracted, flat-field corrected, cleaned of cosmic rays, corrected for bad columns, and wavelength and flux calibrated using MIDAS. Each spectrum was rebinned using the wavelength solution obtained from the corresponding arc-lamp spectrum. All the galaxy and stellar spectra

[1] The Munich Image Data Analysis System (MIDAS) is developed and maintained by the European Southern Observatory (ESO).

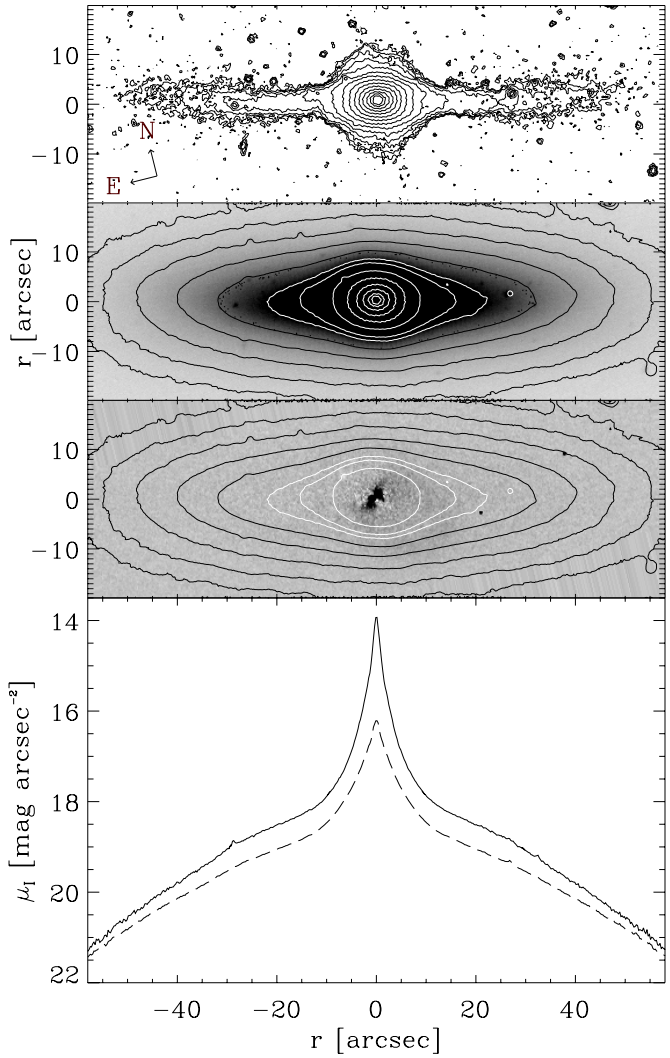

Fig. 1. Surface-brightness distribution of IC 5181. The unsharp masked image, the continuum-band image with some I-band isophotal contours (ranging from 14.7 to 21.6 mag arcsec^{-2} with an increment of 0.6 mag arcsec^{-2}), the continuum-free Hα+[N II] image with I-band isophotal contours (same levels as above), and the radial profiles of the surface brightness extracted along the major axis (solid line) and over a rectangular aperture with a width of 40″ parallel to the major axis and centered on the galactic nucleus (dashed line) are shown (*from top to bottom*). The orientation of the field of view is given in the *top panel*.

were corrected for CCD misalignment. The sky contribution was determined by interpolating along the outermost 10″−30″ at the two edges of the slit, where the galaxy or stellar light was negligible, and then subtracted. A sky subtraction better than 1% was achieved. Each spectrum was flux-calibrated using the sensitivity function as obtained from the flux standard star spectrum of the corresponding night. The spectra obtained for the same galaxy along the same axis were co-added using the center of the stellar continuum as a reference, thus improving the signal-to-noise ratio (S/N) of the final two-dimensional spectrum.

The stellar kinematics are measured from the galaxy absorption features present in the wavelength range and centered on the Mg I line triplet ($\lambda\lambda$ 5164, 5173, 5184 Å) using the Gas and Absorption Line Fitting (GANDALF; Sarzi et al. 2006) IDL[2] code adapted for dealing with the spectra of the 1.52-m ESO telescope. The galaxy spectra were rebinned along the dispersion direction to a logarithmic scale and along the spatial direction to obtain a $S/N \geq 25$ per resolution element. At each radius, a linear combination of template stellar spectra from the MILES library by Sánchez-Blázquez et al. (2006) was convolved with the line-of-sight velocity distribution (LOSVD) and fitted to the observed galaxy spectrum by χ^2 minimization in pixel space. The LOSVD was assumed to be a Gaussian plus third- and fourth-order Gauss-Hermite polynomials, which describe the asymmetric and symmetric deviations of the LOSVD from a pure Gaussian profile (van der Marel & Franx 1993; Gerhard 1993). This allowed us to derive the radial profiles of the line-of-sight velocity, velocity dispersion, and third- and fourth-order Gauss-Hermite moments of the stellar component.

The ionized-gas kinematics were measured with GANDALF from the emission lines present in the spectra, namely Hβ, [O III] $\lambda\lambda$4959, 5007, [N II] $\lambda\lambda$6548, 6583, Hα, and [S II] $\lambda\lambda$6716, 6731. The low S/N of the stellar continuum prevented us to use GANDALF for measuring the gas kinematics for $|r > 17''|$ along the galaxy minor axis. In this radial range, the lines of the [N II] doublet and Hα were fitted by Gaussians, while describing the stellar continuum with a low-order polynomial. We averaged adjacent spectral rows to increase the S/N of the relevant emission lines. The Gaussians were assumed to share the same velocity and velocity dispersion, which correspond to the line-of-sight velocity and velocity dispersion of the ionized gas, respectively. A flux ratio of 1:2.96 was assumed for the [N II] doublet, as dictated by atomic physics (e.g., Osterbrock 1989). The best-fitting Gaussian parameters were derived using a non-linear least-squares minimization based on the robust Levenberg-Marquardt method using the MPFIT algorithm (Markwardt 2009) under the IDL environment as done in Pizzella et al. (2008). This allowed us to trace the radial profiles of the line-of-sight velocity and velocity dispersion of the ionized-gas component.

The uncertainties on the kinematic parameters of the stars and ionized gas were estimated by rescaling the formal errors given as outputs from the least-squares fitting routines to a reduced $\chi^2 = 1$.

The Mg, Fe and Hβ line-strength indices along the major and minor axes were measured following Morelli et al. (2012b). The flux-calibrated spectra were rebinned in the radial direction to achieve a $S/N \geq 50$ per resolution element. The spatial binning is therefore different from the one used for the kinematical measurements. The average iron index, $\langle \mathrm{Fe} \rangle = (\mathrm{Fe5270} + \mathrm{Fe5335})/2$ (Gorgas et al. 1990), and the combined magnesium-iron index, $[\mathrm{MgFe}]' = \sqrt{\mathrm{Mg}\,b\,(0.72 \times \mathrm{Fe5270} + 0.28 \times \mathrm{Fe5335})}$ (Thomas et al. 2003) were computed too. Errors on indices were derived from photon statistics and CCD readout noise and calibrated by means of Monte Carlo simulations. The contamination of the Hβ line-strength index by the Hβ emission line due to the ionized gas present in the galaxy is a problem when deriving the properties of the stellar populations. To address this issue, the Hβ index was measured from the galaxy spectrum after subtracting the contribution of the Hβ emission line. Only Hβ emission lines detected with a $S/N > 3$ were subtracted from the observed spectra.

The stellar kinematics, ionized-gas kinematics, and the line-strength indices measured along the major and minor axis of IC 5181 are plotted in Figs. 2 and 3, respectively. The kinematical measurements are available in Tables 1 and 2 for the stellar and ionized gas, respectively. The line-strength indices measurements are available in Table 3.

[2] The Interactive Data Language (IDL) is distributed by ITT Visual Information Solutions.

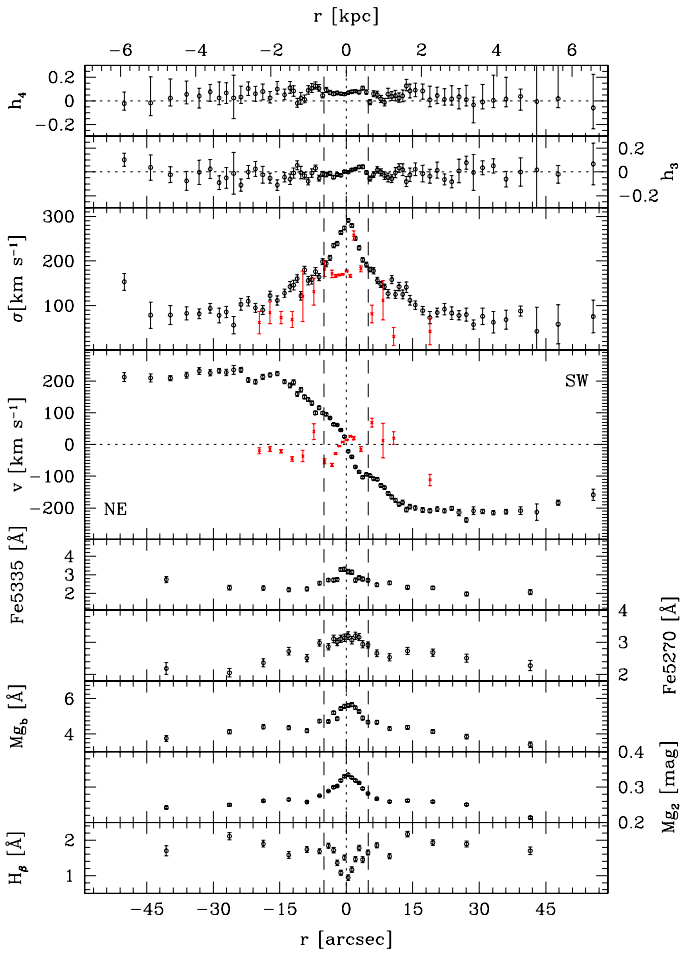

Fig. 2. Kinematic parameters of the stars (circles), ionized gas (crosses), and the line-strength indices as measured along the major axis of IC 5181 (PA = 74°). The radial profiles of the line-of-sight fourth- and third-order coefficient of the Gauss-Hermite decomposition of the LOSVD (h_4 and h_3), velocity (v) after the subtraction of systemic velocity, velocity dispersion (σ), and the line-strength indices Fe5335, Fe5270, Mgb, Mg$_2$, and Hβ are plotted (*from top to bottom*). The vertical dashed lines correspond to the radii ($|r| = r_{\rm bd}$), where the surface-brightness contributions of the bulge and disk are equal.

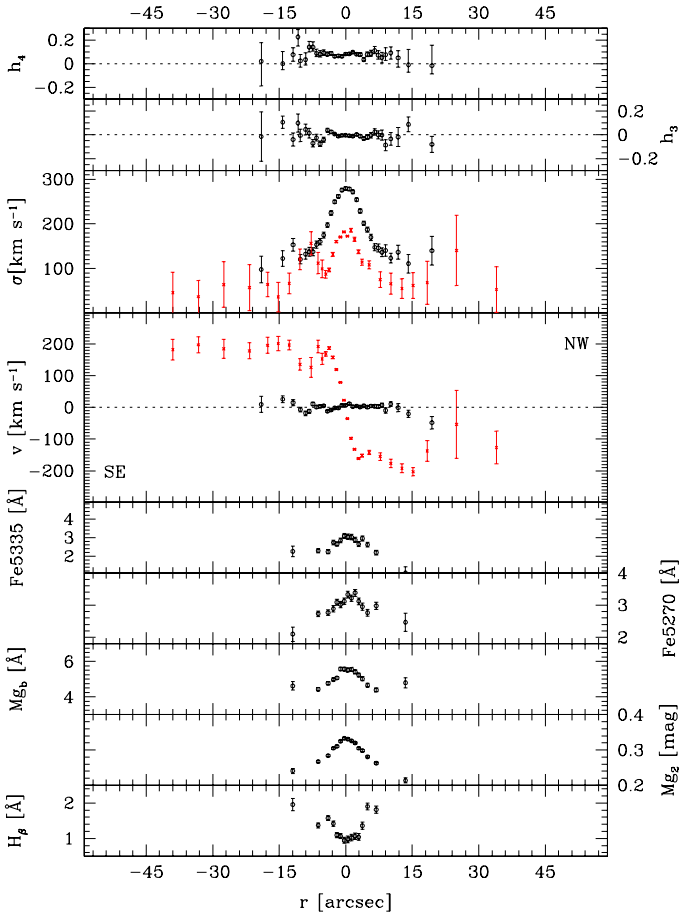

Fig. 3. As in Fig. 2 but for the minor axis of IC 5181 (PA = 164°).

3. Results

3.1. Surface photometry

Isophote-fitting with ellipses, after masking foreground stars and residual bad columns, is carried out on the broadband image using the IRAF[3] task, ELLIPSE. First, isophotes are fitted by ellipses allowing their centers to vary. Within the errors, no variation in the ellipses center is found. Therefore, the final ellipse fits are done at a fixed ellipse center out to a distance of 110″ from the center, where the galaxy surface brightness is larger than 0.5 times the standard deviation of the sky surface brightness. The ellipse-averaged profiles of surface brightness, position angle, and ellipticity are plotted in Fig. 4.

The position angle of the isophotes peaks to 76° at 3″ from the center. At this radius, the ellipticity peaks at 0.22. Further

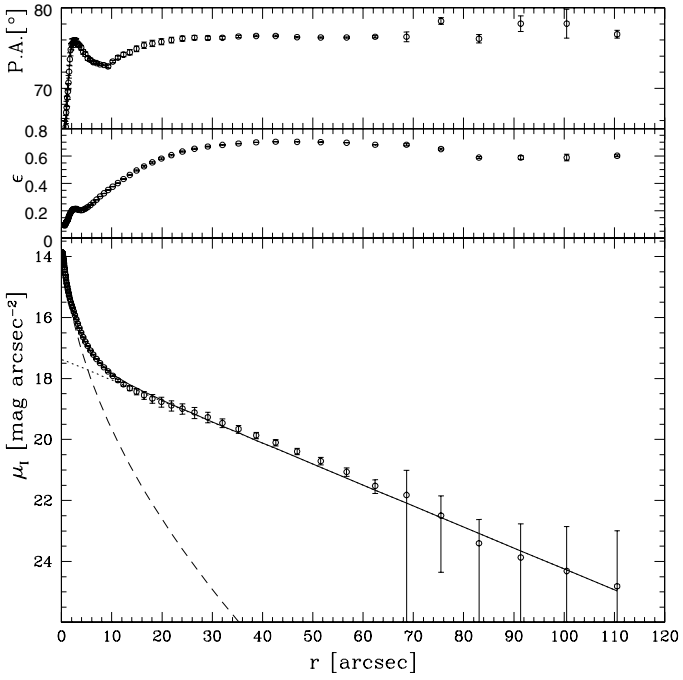

Fig. 4. Isophotal parameters as a function of the semi-major-axis distance and photometric decomposition of IC 5181. The radial profiles of position angle (PA), ellipticity (ϵ), and Cousins I-band surface brightness (μ_I) are plotted (*from top to bottom*). The dashed, dotted, and solid lines represent the surface-brightness radial profiles of the bulge, disc, and model obtained from the photometric decomposition, respectively.

[3] The Imaging Reduction and Analysis Facility (IRAF) is distributed by the National Optical Astronomy Observatory, which is operated by the Association of Universities for Research in Astronomy (AURA), Inc., under cooperative agreement with the National Science Foundation.

out, the position angle and ellipticity decrease to PA = 73° at 10″ and $\epsilon = 0.20$ at 4″, respectively. At larger radii, both the position angle and ellipticity smoothly increase. The position angle reaches a constant value of 76° at radii larger than 25″; the ellipticity rises to a maximum 0.70 at 45″ and then decreases to 0.60 at the outermost observed point. The total magnitude of IC 5181 ($I_T = 10.07 \pm 0.18$) is obtained by extrapolating the surface-brightness radial profile. Our measurements are fully consistent with those by Ho et al. (2011).

The observed change in the position angle of the isophotes between 3″ and 15″ is not expected for an S0 galaxy hosting an axisymmetric bulge. Therefore, a two-dimensional photometric decomposition of the surface-brightness distribution of IC 5181 is performed to better investigate the structure of the galaxy. Two different parametric fitting algorithms are used to this aim, but neither GALFIT (Peng et al. 2010) nor GASP2D (Méndez-Abreu et al. 2008) return a reliable description of the galaxy. Adding one or more extra axisymmetric components or adopting a thick disk do not improve the result. This suggests the presence of a non-axisymmetric component (either a bar or a triaxial bulge), which cannot be properly decomposed due to the high inclination of the galaxy.

Following Bureau et al. (2006), the unsharp-masked image of the broadband frame is built to first gauge the structure and extent of such a non-axisymmetric structure (Fig. 1). The unsharp-mask image is obtained by median-filtering the broadband image, i.e. by replacing the value of each pixel by the difference between it and that of the median within a centered circular aperture of 9″. The size of the aperture is held fixed across the image, but it is chosen to best highlight the features of interest. The surface-brightness distribution of the unsharp-masked image is remarkably similar to that of the median-filtered image of the *N*-body simulations performed by Athanassoula (2005) to investigate the light distribution of a strong bar seen end on.

In addition, the continuum-subtracted image shows the presence of a faint and featureless ionized-gas emission within the inner 6″ from the galaxy center (Fig. 1). The flux of the ionized-gas emission is only a few percens with respect to that of the underlying continuum, and the gaseous structure is elongated almost perpendicularly with respect to the galaxy major axis.

We decide to perform a standard one-dimensional photometric decomposition similar to that adopted by several authors (e.g., Kormendy 1977; Prieto et al. 2001; Méndez-Abreu et al. 2008) to interpret the radial trends of the kinematic and chemical properties measured for the stars and ionized gas in IC 5181. The radial profile of the surface brightness is modeled as the sum of the contribution of a Sérsic bulge and an exponential disk. The effective surface brightness μ_e, effective radius r_e, and shape parameter n of the bulge and the central surface brightness μ_0 and scale-length h of the disk are estimated by minimizing χ^2 of the surface brightnesses in counts pixel^{-1} using the MPFIT algorithm. Each data point is weighted according to the variance of its total observed counts due to the contribution of both galaxy and sky. Each point is determined by assuming photon noise limitation and taking the detector gain and read-out noise into account. Seeing effects are also taken into account by convolving the model surface brightness with a Gaussian PSF with an *FWHM* matching the observed one. The convolution is performed as a product in the Fourier domain before the least-squares minimization. The uncertainties on the structural parameters are estimated by rescaling the formal errors of the fit to a reduced $\chi^2 = 1$. The best-fitting values and their 1σ errors are $\mu_e = 16.8 \pm 0.1$ mag arcsec^{-2}, $r_e = 3\farcs4 \pm 1\farcs4$, $n = 1.89 \pm 0.09$ for the bulge, $\mu_0 = 17.4 \pm 0.1$ mag arcsec^{-2}, and $h = 15\farcs8 \pm 0\farcs2$ for the disk. The bulge-to-disk luminosity ratio $B/D = 0.6$ is derived from the total luminosity after subtracting the disk contribution. The bulge and disk provide the same contribution to the total surface brightness at $r_{bd} = 5''$. The result of the photometric decomposition is shown in Fig. 4. As far as the other structural parameters of the galaxy concern, the innermost peak values of the isophotal position angle and ellipticity are adopted as the observed axial ratio ($q_b = 1 - \epsilon_b = 0.78$) and position angle ($PA_b = 76°$) of the bulge, whereas the observed axial ratio ($q_d = 1 - \epsilon_d = 0.30$) and position angle ($PA_d = 76°$) of the disk are determined by averaging the outer isophotes ($r > 40''$). The disk inclination ($i = 77°$) is calculated by assuming an intrinsic axial ratio of $q_0 = 0.21$ (Padilla & Strauss 2008).

3.2. Stellar and ionized-gas kinematics

The stellar kinematics are measured out to more than 50″ on both sides along the galaxy major axis (Fig. 2). The velocity curve of the stars is characterized by a steep gradient in the bulge-dominated region ($|r| < 5''$), which rises to a maximum observed rotation of about 220 km s^{-1} at a distance of about 15″. At larger radii, the velocity is almost constant, or declining in the two farthest radii as measured on the approaching SW side. The stellar velocity dispersion peaks to a maximum of about 300 km s^{-1} in the center. Further out, it decreases reaching a constant value of 80 km s^{-1} for radii larger than 15″. The major-axis velocity curve of the ionized gas has a more uncertain behavior. It is asymmetric and extends only out to 20″ from the center. The gaseous component counter-rotates with respect to the stars in the bulge-dominated region but the observed rotation velocity is small ($\lesssim$50 km s^{-1}) and declines to zero at larger radii. The gas velocity dispersion is roughly constant at about 170 km s^{-1} for $|r| < 4''$ and decreaes to about 60 km s^{-1} outwards.

The stellar kinematics extends to about 20″ on each side of the nucleus along the galaxy minor axis (Fig. 3). No rotation is measured for the stars and their velocity dispersion falls from a central value of 300 km s^{-1} at about 100 km s^{-1} at the last observed radius. The kinematics of the ionized gas was measured out to larger radii and is characterized by a sharp rotation. The gas velocity rises to about 180 km s^{-1} in the inner 3″. Outwards, it remains constant out at about 40″ on the SE side, whereas it rises and declines on the NW side. The gas velocity dispersion displays a central peak of about 180 km s^{-1}, which falls to an almost constant value of 60 km s^{-1} for $|r| > 10''$.

The analysis of the interplay between the kinematics of the ionized-gas and stars along both the major and minor axis of IC 5181 shows that its gaseous and stellar components are kinematically decoupled to each other and that their projected rotation axes are almost perpendicular.

3.3. Stellar populations

The line-strength indices Fe5335, Fe5270, Mg*b*, and Mg_2 are measured along the major axis peak in the center and decrease to an almost constant value for $|r| > r_{bd}$. Conversely, the radial profile of Hβ shows a central minimum and increases outwards (Fig. 2). This is likely to be due to differences of the stellar populations of bulge and disk, which mostly contribute to the galaxy surface brightness within and outside r_{bd}, respectively (Fig. 4). Indeed, the radial profiles of the line-strength indices do not show any flat portion along the minor axis (Fig. 3), where the

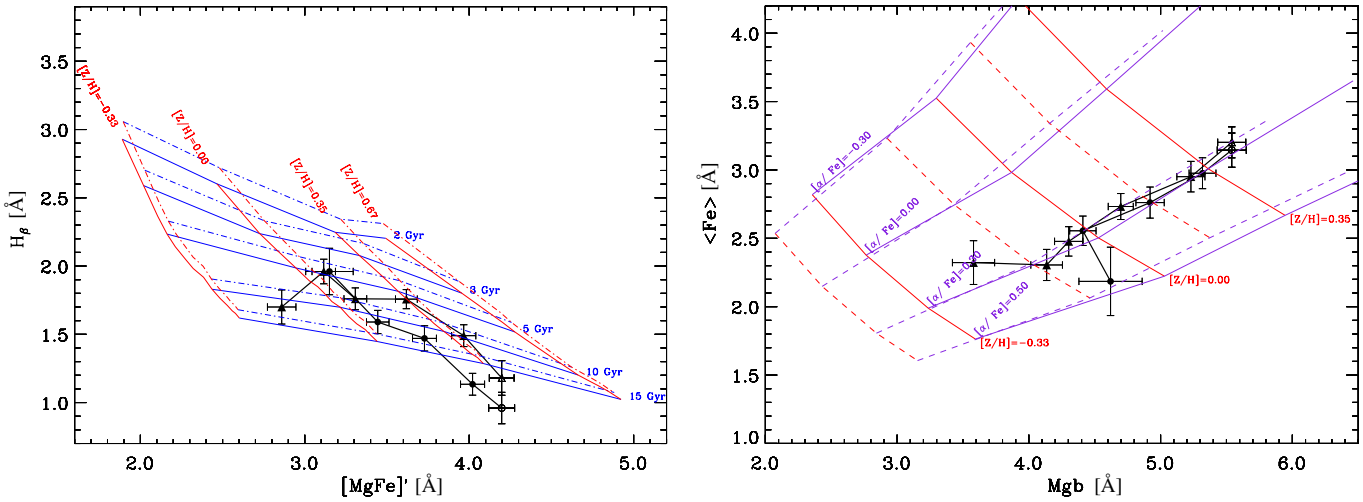

Fig. 5. Hβ and [MgFe]′ indices (*left panel*) and ⟨Fe⟩ and Mg*b* indices (*right panel*) measured along the major (triangles) and minor axis (circles). The open symbols correspond to the values measured in the center of the galaxy and the black lines connect values measured in adjacent radial bins. The radial bins are centered at $r = 0''$, $2''.5$, $5''.5$, $11''.3$, $23''.0$, and $41''.0$ along the major axis and at $r = 0''$, $1''.9$, $3''.9$, $6''.5$ and $11''.9$ along the minor axis. The grids indicate the models by Thomas et al. (2003). In the *left panel* the age-metallicity grids are plotted with two different $[\alpha/\mathrm{Fe}]$ enhancements: $[\alpha/\mathrm{Fe}] = 0.0$ dex (solid lines) and $[\alpha/\mathrm{Fe}] = 0.5$ dex (dashed lines). In the *right panel* the $[\alpha/\mathrm{Fe}]$ ratio-metallicity grids are plotted with two different ages: 8 Gyr (solid lines) and 12 Gyr (dashed lines).

galaxy light is less significantly contaminated by the disk contribution due to its high inclination.

Usually, diagrams of different pairs of line-strength indices are adopted for studying the properties of stellar populations. Here, we use the line-strength indices Hβ, ⟨Fe⟩, and Mg*b* measured in Sect. 2, as performed in Morelli et al. (2012b). Balmer lines of hydrogen are the most sensitive probes of the main sequence turn off temperature (Worthey 1994), while the metal lines (like Mg*b* and ⟨Fe⟩) probe the temperature of the red giant branch (Trager et al. 2000) and the abundances of these elements. The models of Thomas et al. (2003) predict the values of these line-strength indices as a function of the mean age t, total metallicity $[Z/\mathrm{H}]$, and total $[\alpha/\mathrm{Fe}]$ enhancement of a single stellar population.

In Fig. 5, we compare the prediction of the single stellar population models and the line-strength measurements of Hβ, ⟨Fe⟩, and Mg*b* that we obtained by folding their radial profiles and averaging contiguous measurements. The radial bins were centered at $r = 0''$, $2''.5$, $5''.5$, $11''.3$, $23''.0$, and $41''.0$ along the major axis and at $r = 0''$, $1''.9$, $3''.9$, $6''.5$ and $11''.9$ along the minor axis.

In the left panel of Fig. 5, the values of Hβ and [MgFe]′ are compared with the model predictions for two stellar populations with solar ($[\alpha/\mathrm{Fe}] = 0$ dex) and super-solar $[\alpha/\mathrm{Fe}]$ enhancement ($[\alpha/\mathrm{Fe}] = 0.5$ dex), respectively. In this parameter space, the mean age and total metallicity appear to be almost insensitive to the variations of the $[\alpha/\mathrm{Fe}]$ enhancement. In the right panel of Fig. 5, the values of Mg*b* and ⟨Fe⟩ are compared with the model predictions of Thomas et al. (2003) for two stellar populations with old (8 Gyr) and very old age (12 Gyr), respectively. In this parameter space, the total metallicity and total $[\alpha/\mathrm{Fe}]$ enhancement appear to be almost insensitive to the variations of the ages.

The stellar populations in the very center of IC 5181 are very old ($t \sim 15$ Gyr). The values of the age measured along both the major and minor axis are consistent within errors. Along the major axis, the age decreases from 15 to 5 Gyr going from the central to the outer ($r > r_{\mathrm{bd}}$) regions of the galaxy where the disk contribution starts to dominate the galaxy light. This is an indication that the stellar population of the disk is younger than that of the bulge and it has a lower metallicity. This result is consistent with the findings by MacArthur et al. (2009) for a sample of eight spiral galaxies. No clear differences are found for the $[\alpha/\mathrm{Fe}]$ enhancement between the bulge- and disk-dominated regions. As expected for an edge-on galaxy, the disk contamination is significantly smaller along the minor axis on account of the inclination of the galaxy.

The metallicity in the bulge-dominated region has a super-solar value in the center ($[Z/\mathrm{H}] = 0.38$ dex) as it results from the values measured along both major and minor axes. It is characterized by a negligible gradient in the inner $6''$ along the major axis ($\Delta[Z/\mathrm{H}] = -0.06$ dex). In the disk-dominated region the metallicity decreases to reach a value of ($[Z/\mathrm{H}] = -0.18$ dex) at about $40''$. The $[\alpha/\mathrm{Fe}]$ enhancement displays a constant super-solar value ($[\alpha/\mathrm{Fe}] = 0.30$ dex) along both the major and minor axes.

The absence of radial gradients for both metallicity and $[\alpha/\mathrm{Fe}]$ enhancement in the inner regions of IC 5181 ($r < r_{\mathrm{bd}}$) suggests a bulge formation through merging events (Bekki & Shioya 1999) with a very short timescale ($\Delta t \simeq 0.5$ Gyr) for the last burst of star formation (Thomas et al. 2005), which probably happened at the same epoch of the merging.

3.4. Ionized-gas metallicity

To better characterize the nature of the ionized gas, we investigate its metal content and compare it to the stellar component metallicity.

We first have to disentangle the different sources of ionization. With this aim, we use the BPT diagnostic diagrams (Baldwin et al. 1981) adopting the [O III] λ5007/Hβ, [N II] λ6583/Hα, and [S II]/Hα ratios. The emission line fluxes and their ratios are measured along the minor axis on the same spatial bins adopted for the measurements of the line-strength indices. Data are folded around the center, and we average the line ratios measured at similar radii on the two sides of the galaxy. The errors are computed as the RMS of the average. The results are shown in Fig. 6.

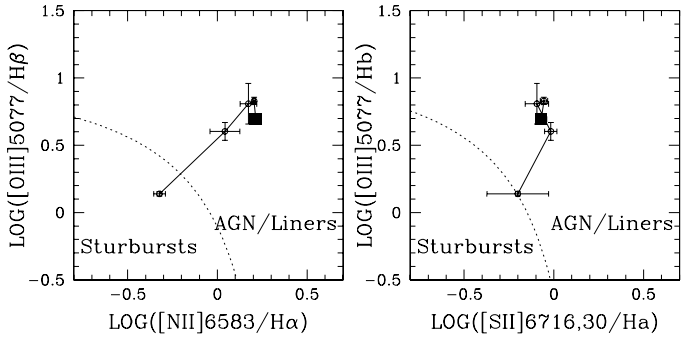

Fig. 6. The BPT diagnostic diagrams from the emission line ratios measured along the minor axis of IC 5181. The radial bins are the same as in Fig. 5. The larger squares mark the values measured in the central radial bin. The solid line connects the measurements from the central to the outermost radial bin. The dotted lines separate the regions occupied by starbursts and AGN/Liners and are taken from Kewley et al. (2001).

The value of [N II] λ6583/Hα = 1.6 found in the central regions is consistent with Phillips et al. (1986) and suggests a Seyfert-type ionization mechanism. However, the last measured points on both sides ($|r|$ = 12″) fall on the limit of the starburst region of the BPT diagram, implying that the ionization due to star formation is dominant in the outer part of the gaseous disk. Therefore we derive the gas-phase metallicity 12 + log (O/H) from the empirical relation with the emission-lines ratio parameter R_3 (Liang et al. 2006) only for this region. In our study we replaced the intensity of the nebular lines Hβ and [O III] $\lambda\lambda$4959, 5007 with their equivalent widths following the prescriptions by Kobulnicky & Phillips (2003). This method has the advantage of being insensitive to reddening. Thus, the equivalent width of the Hβ and [O III] $\lambda\lambda$4959, 5007 emission lines have been measured in the two radial bins at r = ±12″on the minor-axis spectrum. For each emission line, a central bandpass, which covers the feature of interest and two adjacent bandpasses at the red and blue side and traces the local continuum was defined following González (1993) as done in Morelli et al. (2012a). The continuum level underlying the emission line is estimated by interpolating a straight line in the continuum bandpasses of the spectra. The errors associated with the measured equivalent widths are derived from photon statistics and CCD read-out noise, and calibrated by Monte Carlo simulations.

We have obtained a value for the gas-phase metallicity of 12 + log (O/H) = 8.6 ± 0.1 corresponding to a $\langle[Z/H]\rangle_{gas}$ = −0.08 ± 0.07 dex, which was obtained as done by Sommariva et al. (2012) and Coccato et al. (2013). The latter allows a straightforward comparison to the metallicity of the stellar populations in the disk region. The metal content of the ionized gas is barely lower with respect to the stars ([Z/H] = 0.07 ± 0.08). We remark that we apply the above analysis to the measurement done at $|r|$ = 12″, where the emission lines are mainly due to star formation but contamination by AGN/Liners is present. The small difference between the gas phase and stellar component can be view as an additional suggestion of the external origin of the ionized gas, which is not related to the stars and which could have been captured by IC 5181 during an acquisition event from the surrounding environment or neighboring galaxy.

4. Discussion and conclusions

The morphology of IC 5181 shows no remarkable peculiarity. The galaxy disk has a high inclination with respect to the line of sight (i = 77°) and has a regular stellar body without any evidence of warp or dust lanes. A quantitative analysis of the photometric and spectroscopic properties showed that IC 5181 can be considered a typical S0 galaxy with a classical bulge according to the prescription by Kormendy & Kennicutt (2004). The colour index $g - r$ = 0.74 and total magnitude M_r = −20.76 are within the ranges measured for S0 galaxies by Bernardi et al. (2005; magnitudes are taken from Ho et al. 2011 and transformed to the SDSS photometric system following Jester et al. 2005). The bulge has a central velocity dispersion σ_0 = 285 ± 5 km s^{-1} (derived as the mean of the values measured along the major and minor axis), an absolute magnitude $M_{I,b}$ = −20.82, and an effective radius R_e = 0.4 kpc. It follows the Faber-Jackson correlation and lies on the fundamental plane, similar to most of the bulges of S0 and SB0 galaxies (Aguerri et al. 2005). In addition, it rotates as fast as the bulges of early-type disk galaxies and is consistent with being an isotropic rotator (adopting V_{max}/σ_0 = 0.36 and ϵ_b = 0.22; see Morelli et al. 2004 and Aguerri et al. 2005 for a comparison). The age (15 Gyr), metallicity ([Z/H] = 0.38 dex), and overabundance ([α/Fe] = 0.30 dex) of the stellar populations in the bulge-dominated region match the typical values of passively evolving S0 bulges, as derived by Thomas et al. (2003). Finally, IC 5181 fits within the scatter the Mgb-σ relation for early-type galaxies by Jørgensen (1999, adopting Mg$_2$= 0.333 ± 0.003).

The presence of a velocity gradient along the galaxy minor axis is the kinematic signature that ionized gas is not moving onto circular orbits in a disk that is coplanar to that of the stars. This is confirmed by the narrow-band imaging that shows the distribution of the gas in the innermost regions of IC 5181. Moreover, the short dynamical time (few Myr) we derived for the galaxy regions, where we observe the velocity gradient and the regular velocity field of the ionized gas, implies that it is already settled in an equilibrium configuration (e.g., Bertola et al. 1985). Since the intrinsic shape of bulges is triaxial (Bertola et al. 1991; Méndez-Abreu et al. 2008; Méndez-Abreu et al. 2010) and two equilibrium planes are allowed for the gaseous component (e.g., de Zeeuw & Franx 1989), we can explain the observed kinematics of IC 5181 as due to ionized gas settled on the equilibrium plane perpendicular to the long axis of a triaxial bulge. The ionized gas is in orthogonal rotation with respect to the galaxy disk, and we measure zero velocity (or at least a shallower velocity gradient) along the disk major axis and a sharp velocity gradient along the disk minor axis.

To constrain the orientation of the triaxial bulge, we have derived the orientation of the gaseous disk with respect to the line of sight. With this aim, we have compared the circular velocity v_{circ} obtained from the major-axis stellar kinematics with the rotation velocity of the ionized gas v_{gas} measured along the minor axis. The comparison is restricted where the pressure support of the gas is small, and the gas velocity is therefore supposed to trace the circular velocity (Bertola et al. 1995; Pignatelli et al. 2001; Dalcanton & Stilp 2010). All the observed velocities are subtracted of systemic velocity and folded around the galaxy center. For radii larger than 15″, we have obtained a nearly flat circular velocity curve with v_{circ} = 305 ± 10 km s^{-1} by applying the asymmetric drift correction to the major-axis stellar kinematics, as done by Aguerri et al. (2003) after dealing with the effects of integration along the line of sight following Neistein et al. (1999). The ionized-gas rotation curve was derived from the data measured along the minor axis at radii larger than 8″ where σ_{gas} < 60 km s^{-1}. This curve is flat and shows a constant value v_{gas} = 201 ± 6 km s^{-1}. We deprojected v_{gas} onto v_{circ} as done by Wegner et al. (2012) and assumed that the gaseous

component moves onto circular orbits in an infinitesimally thin disk perpendicular to the galaxy disk. For the gaseous disk, we have derived the inclination (i_{gas} = 41° ± 3°) and position angle of its angular momentum (PA_{gas} = 62° ± 2°). The small difference (ΔPA = 14°) between the position angles of the disk major axis and bulge long axis (which coincides with PA_{gas}) have prevented us to successfully model the surface brightness distribution of the triaxial bulge and properly derive its intrinsic shape and contribution to the total light of the galaxy (e.g., as done by Méndez-Abreu et al. 2010; Corsini et al. 2012).

As an alternative, the gas moves on anomalous orbits in a triaxial bulge (or bar) that is tumbling about its short axis (see van Albada & Sanders 1982; Friedli & Benz 1993, for details). This is the case of the lenticular galaxy NGC 128, which hosts a counter-rotating disk of ionized gas (Emsellem & Arsenault 1997; Chung et al. 2012). Similar to IC 5181, the orientation of the ionized gas is not aligned with the stellar disk. This is due to the presence of a tumbling triaxial bar associated with the peanut morphology. In IC 5181, we do not observe gas in retrograde motion relative to stars at large radii from the galaxy center, where the anomalous gas orbits are expected to be highly inclined with respect to the figure rotation axis, since the triaxial bulge (or bar) is seen close to end-on. In this scenario, the gas is settled into a stable configuration and forms a strongly warped disk, whose innermost portion corresponds to an inner polar disk (Corsini et al. 2003; Sil'chenko & Afanasiev 2004). For IC 5181, there is no evidence of stars associated with the orthogonally-rotating gas from either the observed kinematics or the analysis of the stellar populations.

Disentangling between the two alternative geometric configurations with either the innermost or the entire ionized-gas component in orthogonal rotation with respect to the stellar disk requires the analysis of the full velocity field of the galaxy measured with integral-field spectroscopy (Coccato et al. 2007). Nevertheless, the kinematical decoupling between the gaseous and stellar components of IC 5181 suggests the occurrence of an accretion event or merging (Bertola & Corsini 1999). Therefore, it is straightforward to explain the existence of the orthogonally rotating gas in IC 5181 as the end result of the acquisition of external gas by the pre-existing galaxy. The nearby environment of IC 5181 shows no strong evidence of such an event. The galaxy IC 5181 does not interact with its closest companion, NGC 7232A, and is one of the few galaxies of the NGC 7213 group to be undetected in H I (Barnes & Webster 2001). However, all these arguments do not exclude an external origin of the ionized-gas component of IC 5181. Bettoni et al. (2001) proved that the environment of galaxies that experienced past gas accretion do not appear statistically different from those of normal galaxies. In addition, the polar orientation of the ionized gas and its possible low metal content fits well with the scenario proposed for the formation of polar ring galaxies, where the gaseous ring is formed by the accretion of material from a cosmic filament (Macciò et al. 2006; Brook et al. 2008).

Acknowledgements. We thank Michela Mapelli and Marilena Spavone for useful discussions. This work was supported by Padua University through grants 60A02-1283/10, 60A02-5052/11, and 60A02-4807/12. M.C. and L.M. acknowledge financial support from Padua University grant CPDR115539/11 and CPS0204, respectively.

References

Aguerri, J. A. L., Debattista, V. P., & Corsini, E. M. 2003, MNRAS, 338, 465
Aguerri, J. A. L., Elias-Rosa, N., Corsini, E. M., & Muñoz-Tuñón, C. 2005, A&A, 434, 109
Athanassoula, E. 2003, MNRAS, 341, 1179
Athanassoula, E. 2005, MNRAS, 358, 1477
Baldwin, J. A., Phillips, M. M., & Terlevich, R. 1981, PASP, 93, 5
Barnes, D. G., & Webster, R. L. 2001, MNRAS, 324, 859
Bekki, K., & Shioya, Y. 1999, ApJ, 513, 108
Bernardi, M., Sheth, R. K., Nichol, R. C., Schneider, D. P., & Brinkmann, J. 2005, AJ, 129, 61
Bertola, F., & Corsini, E. M. 1999, in Galaxy Interactions at Low and High Redshift, eds. J. E. Barnes, & D. B. Sanders, (Dordrecht: Kluwer), IAU Symp., 186, 149
Bertola, F., Galletta, G., & Zeilinger, W. W. 1985, ApJ, 292, L51
Bertola, F., Vietri, M., & Zeilinger, W. W. 1991, ApJ, 374, L13
Bertola, F., Buson, L. M., & Zeilinger, W. W. 1992, ApJ, 401, L79
Bertola, F., Cinzano, P., Corsini, E. M., Rix, H.-W., & Zeilinger, W. W. 1995, ApJ, 448, L13
Bertola, F., Cinzano, P., Corsini, E. M., et al. 1996, ApJ, 458, L67
Bertola, F., Corsini, E. M., Vega Beltrán, J. C., et al. 1999, ApJ, 519, L127
Bettoni, D., Galletta, G., & Prada, F. 2001, A&A, 374, 83
Brook, C. B., Governato, F., Quinn, T., et al. 2008, ApJ, 689, 678
Bureau, M., Aronica, G., Athanassoula, E., et al. 2006, MNRAS, 370, 753
Burki, G., Rufener, F., Burnet, M., et al. 1995, The Messenger, 80, 34
Chung, A., Bureau, M., van Gorkom, J. H., & Koribalski, B. 2012, MNRAS, 422, 1083
Ciri, R., Bettoni, D., & Galletta, G. 1995, Nature, 375, 661
Coccato, L., Corsini, E. M., Pizzella, A., & Bertola, F. 2007, A&A, 465, 777
Coccato, L., Morelli, L., Pizzella, A., et al. 2013, A&A, 549, A3
Combes, F., Moiseev, A., & Reshetnikov, V. 2013, A&A, 554, A11
Corsini, E. M., Pizzella, A., Coccato, L., & Bertola, F. 2003, A&A, 408, 873
Corsini, E. M., Méndez-Abreu, J., Pastorello, N., et al. 2012, MNRAS, 423, L79
Dalcanton, J. J., & Stilp, A. M. 2010, ApJ, 721, 547
Davis, T. A., Alatalo, K., Sarzi, M., et al. 2011, MNRAS, 417, 882
de Vaucouleurs, G., de Vaucouleurs, A., Corwin, Jr., H. G., et al. 1991, Third Reference Catalogue of Bright Galaxies, 1–3 (New York: Springer)
de Zeeuw, T., & Franx, M. 1989, ApJ, 343, 617
Emsellem, E., & Arsenault, R. 1997, A&A, 318, L39
Emsellem, E., Fathi, K., Wozniak, H., et al. 2006, MNRAS, 365, 367
Friedli, D., & Benz, W. 1993, A&A, 268, 65
Garcia, A. M. 1993, A&AS, 100, 47
Gerhard, O. E. 1993, MNRAS, 265, 213
González, J. J. 1993, Ph.D. Thesis, University of California
Gorgas, J., Efstathiou, G., & Aragon Salamanca, A. 1990, MNRAS, 245, 217
Haynes, M. P., Giovanelli, R., & Chincarini, G. L. 1984, ARA&A, 22, 445
Ho, L. C., Li, Z.-Y., Barth, A. J., Seigar, M. S., & Peng, C. Y. 2011, ApJS, 197, 21
Iodice, E., Arnaboldi, M., Sparke, L. S., Gallagher, J. S., & Freeman, K. C. 2002, A&A, 391, 103
Jester, S., Schneider, D. P., Richards, G. T., et al. 2005, AJ, 130, 873
Jørgensen, I. 1999, MNRAS, 306, 607
Kannappan, S. J., & Fabricant, D. G. 2001, AJ, 121, 140
Katkov, I. Y., Sil'chenko, O. K., & Afanasiev, V. L. 2013, ApJ, 769, 105
Kewley, L. J., Dopita, M. A., Sutherland, R. S., Heisler, C. A., & Trevena, J. 2001, ApJ, 556, 121
Kobulnicky, H. A., & Phillips, A. C. 2003, ApJ, 599, 1031
Kormendy, J. 1977, ApJ, 217, 406
Kormendy, J., & Kennicutt, Jr., R. C. 2004, ARA&A, 42, 603
Krajnović, D., & Jaffe, W. 2004, A&A, 428, 877
Kuijken, K., Fisher, D., & Merrifield, M. R. 1996, MNRAS, 283, 543
Liang, Y. C., Yin, S. Y., Hammer, F., et al. 2006, ApJ, 652, 257
MacArthur, L. A., González, J. J., & Courteau, S. 2009, MNRAS, 395, 28
Macciò, A. V., Moore, B., & Stadel, J. 2006, ApJ, 636, L25
Maia, M. A. G., da Costa, L. N., & Latham, D. W. 1989, ApJS, 69, 809
Markwardt, C. B. 2009, in Astronomical Data Analysis Software and Systems XVIII, eds. D. A. Bohlender, D. Durand, & P. Dowler, ASP Conf. Ser., 411, 251
Matthews, L. D. & de Grijs, R. 2004, AJ, 128, 137
Méndez-Abreu, J., Aguerri, J. A. L., Corsini, E. M., & Simonneau, E. 2008, A&A, 478, 353
Méndez-Abreu, J., Simonneau, E., Aguerri, J. A. L., & Corsini, E. M. 2010, A&A, 521, A71
Moiseev, A. V., Smirnova, K. I., Smirnova, A. A., & Reshetnikov, V. P. 2011, MNRAS, 418, 244
Morelli, L., Halliday, C., Corsini, E. M., et al. 2004, MNRAS, 354, 753
Morelli, L., Calvi, V., Cardullo, A., et al. 2012a, A&A, 544, A74
Morelli, L., Corsini, E. M., Pizzella, A., et al. 2012b, MNRAS, 423, 962
Neistein, E., Maoz, D., Rix, H.-W., & Tonry, J. L. 1999, AJ, 117, 2666
Osterbrock, D. E. 1989, Astrophysics of gaseous nebulae and active galactic nuclei (Mill Valley, CA: University Science Books)
Padilla, N. D., & Strauss, M. A. 2008, MNRAS, 388, 1321

Peng, C. Y., Ho, L. C., Impey, C. D., & Rix, H.-W. 2010, AJ, 139, 2097
Phillips, M. M., Jenkins, C. R., Dopita, M. A., Sadler, E. M., & Binette, L. 1986, AJ, 91, 1062
Pignatelli, E., Corsini, E. M., Vega Beltrán, J. C., et al. 2001, MNRAS, 323, 188
Pizzella, A., Amico, P., Bertola, F., et al. 1997, A&A, 323, 349
Pizzella, A., Corsini, E. M., Vega Beltrán, J. C., & Bertola, F. 2004, A&A, 424, 447
Pizzella, A., Corsini, E. M., Sarzi, M., et al. 2008, MNRAS, 387, 1099
Prieto, M., Aguerri, J. A. L., Varela, A. M., & Muñoz-Tuñón, C. 2001, A&A, 367, 405
Rubin, V. C. 1994, AJ, 108, 456
Rubin, V. C., Graham, J. A., & Kenney, J. D. P. 1992, ApJ, 394, L9
Sánchez-Blázquez, P., Peletier, R. F., Jiménez-Vicente, J., et al. 2006, MNRAS, 371, 703
Sandage, A. & Bedke, J. 1994, The Carnegie Atlas of Galaxies, I, II (Washington, DC: Carnegie Inst. of Washington)
Sarzi, M., Falcón-Barroso, J., Davies, R. L., et al. 2006, MNRAS, 366, 1151
Schweizer, F. 1998, in Saas-Fee Advanced Course 26: Galaxies: Interactions and Induced Star Formation, eds. R. C. Kennicutt, Jr., F. Schweizer, J. E. Barnes, et al. (New York: Springer), 105
Sil'chenko, O. K., & Afanasiev, V. L. 2004, AJ, 127, 2641
Sil'chenko, O. K., Moiseev, A. V., & Afanasiev, V. L. 2009, ApJ, 694, 1550
Sommariva, V., Mannucci, F., Cresci, G., et al. 2012, A&A, 539, A136
Spavone, M., Iodice, E., Arnaboldi, M., et al. 2010, ApJ, 714, 1081
Thomas, D., Maraston, C., & Bender, R. 2003, MNRAS, 339, 897
Thomas, D., Maraston, C., Bender, R., & Mendes de Oliveira, C. 2005, ApJ, 621, 673
Trager, S. C., Faber, S. M., Worthey, G., & González, J. J. 2000, AJ, 120, 165
Tully, R. B. 1988, Nearby galaxies catalog (Cambridge: Cambridge Univ. Press)
van Albada, T. S. & Sanders, R. H. 1982, MNRAS, 201, 303
van der Marel, R. P., & Franx, M. 1993, ApJ, 407, 525
Wegner, G. A., Corsini, E. M., Thomas, J., et al. 2012, AJ, 144, 78
Whitmore, B. C., Lucas, R. A., McElroy, D. B., et al. 1990, AJ, 100, 1489
Worthey, G. 1994, ApJS, 95, 107

Pages 10 to 13 are available in the electronic edition of the journal at http://www.aanda.org

Table 1. Stellar kinematics along the major (PA = 76°) and minor (PA = 164°) axis of IC 5181.

PA	r	$V \pm \mathrm{d}V$		$\sigma \pm \mathrm{d}\sigma$		$h_3 \pm \mathrm{d}h_3$		$h_4 \pm \mathrm{d}h_4$	
°	″	km s^{-1}		km s^{-1}					
76	–50.0	213	14	153	19	0.103	0.056	–0.022	0.096
76	–44.1	210	12	78	30	0.038	0.107	–0.017	0.221
76	–39.6	210	8	79	21	–0.023	0.066	0.023	0.162
76	–36.0	219	9	82	14	–0.075	0.080	0.056	0.111
76	–33.2	232	11	82	11	–0.002	0.102	0.041	0.065
76	–30.7	226	10	94	11	0.025	0.081	0.076	0.064
76	–28.7	233	7	78	17	–0.090	0.058	0.025	0.135
76	–27.0	228	10	86	13	–0.049	0.088	0.068	0.086
76	–25.4	236	14	56	20	–0.012	0.176	0.025	0.191
76	–23.7	236	8	103	13	–0.110	0.052	0.032	0.092
76	–22.1	204	8	110	10	0.000	0.056	0.104	0.056
76	–20.5	198	8	95	10	0.026	0.063	0.061	0.062
76	–18.8	213	8	90	10	–0.023	0.070	0.079	0.063
76	–17.2	220	6	122	10	–0.052	0.042	0.025	0.055
76	–15.5	224	6	112	10	–0.110	0.044	0.100	0.063
76	–13.9	198	6	128	9	–0.044	0.040	0.051	0.048
76	–12.7	186	8	143	12	–0.061	0.045	0.110	0.054
76	–11.9	196	8	146	11	–0.009	0.044	0.083	0.045
76	–11.0	160	7	161	8	0.057	0.036	–0.019	0.039
76	–10.2	173	7	122	10	–0.005	0.052	0.023	0.049
76	–9.4	150	6	180	9	–0.031	0.029	0.013	0.036
76	–8.6	142	6	156	9	–0.079	0.031	0.089	0.040
76	–7.8	131	6	158	10	–0.009	0.035	0.107	0.040
76	–6.9	100	6	176	9	0.032	0.027	0.126	0.034
76	–6.1	116	5	164	8	–0.053	0.025	0.106	0.032
76	–5.3	100	5	199	7	–0.015	0.022	0.046	0.025
76	–4.5	96	4	194	6	–0.021	0.019	0.092	0.023
76	–3.7	84	4	207	6	–0.012	0.016	0.070	0.019
76	–2.8	63	4	235	5	–0.044	0.013	0.058	0.016
76	–2.0	62	3	239	4	–0.020	0.011	0.067	0.014
76	–1.2	46	3	264	4	–0.029	0.009	0.061	0.011
76	–0.4	25	3	274	4	0.004	0.009	0.057	0.010
76	0.4	–21	3	291	4	–0.002	0.008	0.069	0.010
76	1.3	–38	3	280	4	0.019	0.009	0.078	0.011
76	2.1	–70	3	251	4	0.025	0.010	0.082	0.012
76	2.9	–86	3	229	5	0.042	0.013	0.074	0.015
76	3.7	–103	4	203	6	0.044	0.015	0.107	0.019
76	4.5	–94	4	192	5	–0.003	0.017	0.074	0.020
76	5.4	–98	4	181	5	–0.055	0.020	–0.011	0.022
76	6.2	–108	5	178	7	–0.021	0.023	0.060	0.026
76	7.0	–110	5	156	7	0.018	0.026	0.052	0.030
76	7.8	–129	5	148	7	–0.002	0.030	0.017	0.031
76	8.6	–136	5	142	6	–0.030	0.031	–0.013	0.033
76	9.5	–154	6	127	9	–0.047	0.037	0.057	0.049
76	10.3	–166	6	158	9	–0.056	0.033	0.037	0.040
76	11.1	–176	6	125	9	–0.006	0.043	0.044	0.044
76	11.9	–188	6	143	9	0.034	0.036	0.024	0.045
76	12.7	–182	7	125	10	0.020	0.051	0.043	0.050
76	13.6	–206	7	141	12	–0.081	0.043	0.127	0.054
76	14.4	–196	8	112	11	–0.024	0.057	0.083	0.059
76	15.6	–200	6	101	9	0.023	0.054	0.090	0.060
76	17.2	–207	8	89	9	–0.013	0.070	0.083	0.061
76	18.9	–209	6	73	14	–0.035	0.059	0.009	0.115
76	20.5	–204	7	84	10	0.015	0.068	0.045	0.071
76	22.2	–209	6	92	13	–0.063	0.047	0.013	0.090
76	23.8	–201	6	83	14	–0.082	0.052	0.016	0.111
76	25.4	–214	10	78	10	0.009	0.100	0.033	0.069
76	27.1	–238	6	80	15	0.078	0.055	0.011	0.120
76	28.7	–209	12	58	10	–0.004	0.152	–0.033	0.064
76	30.8	–211	6	76	18	0.036	0.058	–0.008	0.147
76	33.2	–215	6	63	24	0.052	0.060	0.004	0.213
76	36.1	–212	7	68	21	–0.059	0.066	0.015	0.184
76	39.3	–209	12	88	12	–0.000	0.118	0.038	0.063
76	43.0	–213	26	42	54	0.018	0.410	–0.006	0.557
76	47.8	–183	8	58	44	–0.019	0.075	0.019	0.389

Table 1. continued.

PA	r	$V \pm dV$		$\sigma \pm d\sigma$		$h_3 \pm dh_3$		$h_4 \pm dh_4$	
°	″	km s^{-1}		km s^{-1}					
76	55.7	–159	18	76	36	0.067	0.177	–0.058	0.282
164	–19.0	10	25	98	30	–0.015	0.208	0.021	0.157
164	–14.2	26	10	122	18	0.107	0.052	0.001	0.101
164	–11.9	15	10	153	14	–0.039	0.055	0.077	0.057
164	–10.2	–7	7	121	10	–0.005	0.052	0.025	0.054
164	–9.0	–18	7	132	12	0.045	0.045	0.035	0.058
164	–8.2	–12	6	138	10	0.014	0.040	0.141	0.049
164	–7.4	11	5	137	9	–0.071	0.032	0.140	0.045
164	–6.6	1	5	153	8	–0.024	0.028	0.088	0.035
164	–5.8	3	4	160	7	–0.076	0.023	0.081	0.031
164	–5.0	5	4	175	6	–0.041	0.020	0.092	0.026
164	–4.1	–12	3	197	5	0.039	0.015	0.081	0.018
164	–3.3	–8	3	225	5	0.026	0.012	0.088	0.015
164	–2.5	–2	3	250	4	0.007	0.010	0.062	0.012
164	–1.7	–2	3	262	4	–0.010	0.009	0.066	0.011
164	–0.8	7	3	276	4	–0.005	0.009	0.062	0.010
164	–0.0	7	3	280	4	–0.003	0.008	0.082	0.010
164	0.8	12	3	278	4	–0.007	0.008	0.083	0.010
164	1.6	3	3	272	4	–0.011	0.009	0.097	0.011
164	2.4	4	3	254	4	0.003	0.010	0.081	0.012
164	3.2	1	3	229	5	–0.010	0.012	0.078	0.015
164	4.1	6	3	202	5	–0.030	0.015	0.035	0.017
164	4.9	1	4	187	6	–0.018	0.018	0.079	0.022
164	5.7	4	4	170	7	–0.003	0.022	0.085	0.028
164	6.5	3	5	148	8	0.025	0.027	0.111	0.036
164	7.4	3	6	146	9	0.001	0.034	0.072	0.039
164	8.8	7	7	136	10	–0.002	0.043	0.051	0.044
164	9.0	–9	8	140	13	–0.087	0.046	0.076	0.061
164	10.2	10	8	123	11	–0.034	0.053	0.092	0.052
164	11.8	–1	13	137	16	–0.018	0.079	0.050	0.059
164	14.1	–20	11	111	21	0.088	0.062	–0.009	0.129
164	19.4	–48	20	140	32	–0.080	0.068	–0.016	0.172

Table 2. Ionized gas kinematics along the major (PA = 76°) and minor (PA = 164°) axis of IC 5181.

PA	r	$V \pm dV$		$\sigma \pm d\sigma$	
°	″	km s^{-1}		km s^{-1}	
76	–19.6	–19	10	62	25
76	–17.2	–14	8	84	25
76	–14.7	–21	6	73	14
76	–12.2	–45	7	69	18
76	–9.8	–37	18	121	57
76	–7.3	41	25	131	30
76	–4.9	–53	8	182	17
76	–3.2	–64	5	172	9
76	–2.4	–29	2	167	4
76	–1.6	–5	1	169	2
76	–0.8	7	1	170	1
76	0.1	15	1	178	2
76	0.9	27	2	167	3
76	1.7	20	5	258	10
76	3.3	–14	8	183	7
76	5.8	69	14	81	20
76	8.3	12	55	112	44
76	10.7	20	20	31	20
76	18.9	–112	18	42	30
164	–39.0	182	32	46	46
164	–33.2	198	25	37	42
164	–27.5	185	30	64	51
164	–21.7	178	25	57	51
164	–17.6	196	25	64	28
164	–15.2	201	22	36	33
164	–12.7	197	15	66	23
164	–10.3	136	18	121	23
164	–7.8	126	31	156	26
164	–6.2	192	20	112	24
164	–5.3	153	17	99	20
164	–4.5	169	7	87	8
164	–3.7	187	4	97	4
164	–2.9	158	4	132	4
164	–2.1	119	2	160	2
164	–1.2	79	1	171	2
164	–0.4	22	1	182	1
164	0.4	–35	1	173	1
164	1.2	–97	2	186	4
164	2.0	–132	2	166	5
164	2.9	–161	2	138	4
164	3.7	–152	5	114	7
164	5.3	–142	7	108	9
164	7.8	–155	12	75	17
164	10.2	–176	13	66	24
164	12.7	–192	14	55	22
164	15.2	–203	13	62	29
164	18.4	–137	32	68	48
164	25.0	–53	108	141	79
164	34.0	–126	52	53	51

Table 3. Line strength measurements along the major (PA = 76°) and minor (PA = 164°) axis of IC 5181.

PA	r	Hβ		Mg_2		Mgb		Fe_{5270}		Fe_{5335}	
°	″	Å ± dÅ		mag ± dmag		Å ± dÅ		Å ± dÅ		Å ± dÅ	
76	–40.6	1.70	0.14	0.242	0.004	3.75	0.17	2.19	0.18	2.75	0.17
76	–26.3	2.11	0.10	0.250	0.003	4.13	0.12	2.05	0.13	2.30	0.12
76	–18.7	1.90	0.10	0.261	0.003	4.41	0.12	2.36	0.12	2.28	0.11
76	–13.0	1.58	0.09	0.265	0.003	4.35	0.11	2.72	0.12	2.19	0.11
76	–8.9	1.74	0.08	0.258	0.003	4.18	0.10	2.51	0.11	2.24	0.10
76	–6.0	1.69	0.07	0.276	0.002	4.73	0.09	2.98	0.10	2.55	0.09
76	–4.0	1.84	0.07	0.289	0.002	4.71	0.09	2.86	0.10	2.72	0.09
76	–2.8	1.72	0.08	0.300	0.003	5.20	0.10	3.11	0.12	2.71	0.11
76	–2.0	1.36	0.08	0.303	0.003	4.86	0.10	3.01	0.11	2.75	0.10
76	–1.2	1.08	0.07	0.319	0.003	5.44	0.10	3.11	0.11	3.28	0.10
76	–0.4	1.51	0.11	0.331	0.003	5.57	0.11	3.14	0.12	3.30	0.11
76	0.4	0.95	0.08	0.335	0.003	5.61	0.11	3.21	0.12	3.17	0.12
76	1.3	1.17	0.08	0.327	0.003	5.66	0.11	3.07	0.12	3.14	0.12
76	2.1	1.46	0.08	0.319	0.003	5.49	0.11	3.20	0.11	2.71	0.11
76	2.9	1.78	0.08	0.312	0.003	5.27	0.11	3.16	0.11	2.84	0.11
76	3.7	1.45	0.08	0.296	0.003	4.90	0.11	2.94	0.11	2.77	0.11
76	4.9	1.65	0.07	0.282	0.002	4.68	0.10	2.92	0.10	2.71	0.09
76	6.9	1.85	0.07	0.267	0.002	4.67	0.10	2.66	0.10	2.46	0.09
76	9.8	1.55	0.07	0.259	0.003	4.30	0.11	2.54	0.11	2.56	0.10
76	13.8	2.17	0.08	0.262	0.003	4.38	0.11	2.73	0.11	2.33	0.10
76	19.6	1.94	0.08	0.259	0.003	4.14	0.12	2.68	0.11	2.29	0.10
76	27.2	1.89	0.08	0.251	0.003	3.86	0.12	2.51	0.12	1.97	0.10
76	41.5	1.70	0.11	0.214	0.004	3.41	0.15	2.28	0.16	2.07	0.13
164	–11.9	1.96	0.17	0.241	0.007	4.62	0.24	2.10	0.22	2.27	0.28
164	–6.2	1.37	0.07	0.267	0.003	4.43	0.09	2.74	0.08	2.30	0.11
164	–4.0	1.58	0.07	0.284	0.003	4.77	0.09	2.77	0.09	2.24	0.11
164	–2.8	1.42	0.07	0.305	0.003	4.98	0.10	2.89	0.09	2.74	0.12
164	–2.0	1.10	0.07	0.310	0.003	5.07	0.09	3.09	0.09	2.66	0.12
164	–1.2	1.07	0.08	0.325	0.003	5.58	0.10	3.02	0.09	2.85	0.13
164	–0.3	0.95	0.10	0.333	0.003	5.56	0.11	3.12	0.10	3.09	0.14
164	0.5	0.97	0.10	0.331	0.003	5.52	0.11	3.33	0.11	3.04	0.15
164	1.3	1.02	0.09	0.326	0.003	5.55	0.11	3.22	0.10	3.03	0.14
164	2.1	1.06	0.09	0.320	0.003	5.41	0.11	3.38	0.11	2.88	0.14
164	2.9	1.04	0.10	0.305	0.003	5.23	0.11	3.12	0.11	2.65	0.13
164	3.8	1.36	0.10	0.298	0.003	5.03	0.12	2.96	0.11	2.96	0.14
164	4.9	1.90	0.10	0.281	0.003	4.65	0.11	2.77	0.10	2.62	0.12
164	6.9	1.81	0.10	0.263	0.003	4.39	0.11	2.98	0.11	2.20	0.13
164	13.5	4.34	0.25	0.214	0.007	4.80	0.28	2.47	0.28	1.11	0.33